Corrosion of aircraft heritage: a comparison between modern and historic Duralumin alloys

Carla Martini[1], Elena Bernardi[2*], Cecilia Velino[2], Luca Lorenzetti[1], Andrea Balbo[3], Federica Zanotto[3], Magali Brunet[4], Luc Robbiola[5], Elodie Guilminot[6] and Cristina Chiavari[7]

Abstract

The development of innovative solutions for the conservation and the protection of historic aircraft is a recent and important issue raised in the cultural heritage field and represents the goal of the PROCRAFT (Protection and Conservation of Heritage Aircraft) project. Assessing and documenting the constituent materials as well as their degradation state is necessary to determine and understand factors inducing aluminium alloy corrosion, in order to develop tailored conservation treatments and identify effective protective coatings. The first step of the project was the identification of the constituent materials of aircraft wrecks. Al-Cu-Mg alloys—Duralumin and Super Duralumin, with a higher content of Mg—were the most employed alloys for structural and non-structural parts. These materials undergo a wide range of alterations, amongst which pitting, exfoliation and galvanic corrosion.

In the present work, results of the characterisation of wrecks from a North American Republic P-47D Thunderbolt, crashed in Italy in 1945, are reported and compared to wrecks from a French Breguet 765 Sahara n°504 64-PH, built in 1958. The constituent alloys resulted to be similar to the modern 2024 and 2017A alloy.

In order to assess the representativeness of these modern alloys in simulating the corrosion behaviour of the historic ones, exfoliation susceptibility (ASTM G34) as well as non-destructive and destructive electrochemical tests in 0.1 M NaCl were carried out on both historic and modern alloys. These results contributed to the selection of representative substrates for the development of protective coatings as well as to the expansion of the dataset on composition and microstructure of historic Al alloys for aircraft.

Keywords Aluminium alloys, Microstructure, Corrosion, Historic aircraft, Conservation cultural heritage

*Correspondence:
Elena Bernardi
elena.bernardi@unibo.it
[1] Department of Industrial Engineering, University of Bologna, viale Risorgimento 4, 40136 Bologna, Italy
[2] Department of Industrial Chemistry "Toso Montanari", University of Bologna, viale Risorgimento 4, 40136 Bologna, Italy
[3] Corrosion and Metallurgy Study Centre "Aldo Daccò", University of Ferrara, Via G. Saragat 4a, 44122 Ferrara, Italy
[4] CEMES-CNRS, Université de Toulouse Jean Jaurès, 29 rue Jeanne Marvig, 31055 Toulouse, France
[5] TRACES, CNRS UMR 5608, Université de Toulouse Jean Jaurès, 31100 Toulouse, France
[6] Arc'Antique, Grand Patrimoine de Loire Atlantique, 26 rue de la Haute Forêt, 44300 Nantes, France
[7] Department of Cultural Heritage, University of Bologna, via degli Ariani 1, 48121 Ravenna, Italy

Introduction

Despite its undeniable historic importance, the study of twentieth-century aircraft has only recently entered the field of archaeology and cultural heritage conservation [1]. A systematic approach regarding the conservation of historic aircraft is currently missing. To fill this gap, the JPI-CH PROCRAFT project (2020–23) aims to develop innovative and integrated strategies for restoration and conservation of WWII aeronautical wrecks following a global approach "from excavation to museums". PROCRAFT takes care of all the key steps involved in long-term aircraft conservation in outdoor and indoor environments. Most aircrafts from the last century were built using aluminium-based materials and the characterisation of the constituent phases in the alloys was the

Martini *et al. Heritage Science*   (2024) 12:16

Page 2 of 21

first step of the research, which allowed the identification and characterisation of historic wrecks from several nations: Germany, France, Italy, USA, UK, and USSR [2]. On the basis of this extensive survey, Al-Cu-Mg alloys—Duralumin and Super Duralumin, with a higher content of Mg—resulted the most employed alloys for structural and non-structural parts [3]. The modern alloys 2024 and 2017A were identified as the most closely representative of ancient ones, in terms of composition and microstructure [2].

The identification of modern representative alloys is a key point for setting up effective and long-term conservation treatments of these cultural heritage metals. As a consequence, the development of protective coatings for conservation of the ancient alloys requires both (i) the comprehension of corrosion mechanisms which affected historic materials and (ii) the capability to test the developed coatings on representative substrates.

As regards point (i), even though the degradation of Al alloys is widely studied in various atmospheric environmental conditions [4–6] as well as in sea water [7–11], underground Al corrosion, often occurring in aircraft wrecks, has not been extensively investigated. In general, aluminium and its alloys can undergo different types of corrosion [12, 13], most of which are due to the presence of microstructural heterogeneities: intermetallic particles, such as precipitates, constituent phases and dispersoids are known to be the sites where localised attack begins [14–17]. Their different chemical composition from the Al-rich matrix results in micro-galvanic interactions [18] that leads to local dissolution of the surrounding matrix along the particle borders (known as trenching [19]). However, recent studies provided deeper insight regarding the role of specific intermetallic particles in the corrosion process, investigating at nanometric scale the dissolution mechanisms of the most common particles found in Al-Cu-Mg alloys [19–21]. Another common corrosion process occurring in Al alloys is exfoliation, which occurs in aluminium alloys with marked directional microstructures [22]. Exfoliation corrosion is a form of localized corrosion that propagates intergranularly along the rolling or extrusion direction. Swelling of alloys occurs due to the formation of bulky corrosion products that induce stress at the grain boundary. Mechanical actions or abrasion tend to remove the lifted grains, thus exposing the underlying ones and triggering the exfoliation process [23]. This type of corrosion, typical of Al-Cu-Mg alloys, is often observed in aircraft components exposed to aggressive, chloride-rich environments (such as de-icing salts, seacoast atmosphere or deep sea) [24], especially around riveted or bolted components, where the surface discontinuity offers suitable propagation sites.

The aim of this work is twofold: (i) investigation of the composition, microstructure and corrosion behaviour of Aluminium-based materials from a US aircraft (Republic P47-D Thunderbolt, crashed on land in Italy on April 21st, 1945 and excavated by volunteers in 2016 [25]) as well as of fragments from the wreck of a French Breguet 765 Sahara n°504 64-PH, and (ii) assessment of the feasibility to use modern Al-alloys as representative substrates for testing protective coatings and treatments.

The first aim is to collect further data for the corpus of wrecks documented within the PROCRAFT project and gain further knowledge on materials and materials degradation in WWII aircraft. Previous studies carried out in PROCRAFT revealed that most Al-based materials in WWII aircraft consisted of Duralumin (comparable with modern 2017A) and/or Super-Duralumin (comparable to modern 2024). In fact, the identification of alloys representative of the historic materials is mandatory for achieving reliable and transferable results without wasting the original and unique artifacts.

The representativeness of modern alloys in terms of corrosion behaviour was evaluated firstly by exfoliation tests (EXCO, ASTM G34-01 [26]) as a preliminary screening tool for the comparison of historic and modern alloys, followed by a combination of (i) electrochemical tests (potentiodynamic polarisation and electrochemical impedance spectroscopy, EIS) for comparing 2017A-like alloys, using samples belonging to the Duralumin family from the wreck of a 765 Sahara by Breguet, France [27, 28] and (ii) accelerated ageing tests for investigating localised corrosion phenomena triggered by intermetallic particles in 2024-like alloys.

Materials and methods

The historic fragments from the Thunderbolt P-47D by Republic Aviation Co.,USA (Sect. "Thunderbolt P-47D"), as well as samples from a 765 Sahara by Breguet, France (Sect. "Breguet 765 Sahara") and samples from modern alloys (Sect. "Modern Alloys"), were characterised in terms of composition, microstructure, hardness and corrosion features (Sect. "Materials characterisation"). Samples from these airplanes, together with samples from modern alloys, were also prepared for corrosion testing.

For the EXCO test (Sect. "Exfoliation test"), samples were cut to obtain flat specimens of about 2×2 cm^2, surface-polished with abrasive paper (1000 grit). At the end of the EXCO test, specimens were embedded in epoxy resin and polished by conventional metallographic procedures for cross-section observations.

The corrosion behaviour was investigated by electrochemical characterisation of both modern and historic alloys applying electrochemical impedance spectroscopy

Martini *et al. Heritage Science* (2024) 12:16

Page 3 of 21

(EIS) and potentiodynamic tests (Sect. "Electrochemical tests").

For localised ageing tests (Sect. "Localised ageing tests"), specimens (approximately 0.5×1 cm^2) were embedded in epoxy resin and polished with abrasive paper (1200 grit) followed by abrasive diamond paste (9, 3 and 1 μm).

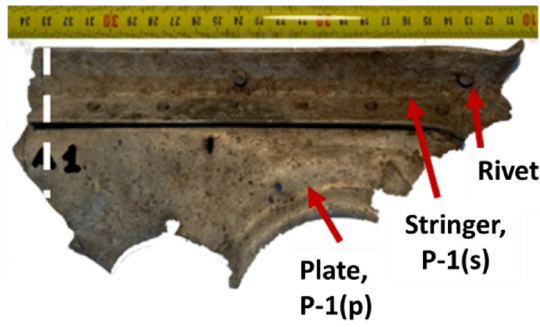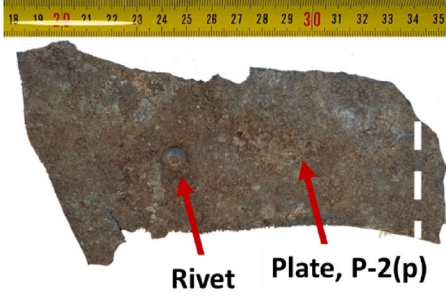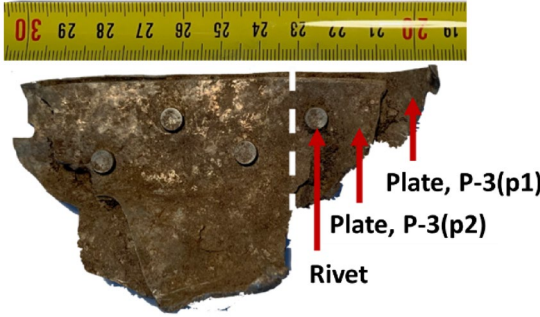## Characterisation of constituent materials
Thunderbolt P-47D
Fragments from the wreck of a Thunderbolt P-47D aircraft crashed in Bagnarola near Bologna on April 21st, 1945 due to German ground anti-aircraft fire were provided by the association "Air Club & Fun" in Argelato, Bologna (Italy). The heavily deformed and damaged wreck was excavated from slightly boggy, clay-based soil (about 15 feet underground) in July 2016. Pieces from both the fuselage skin and the support structure were classified according to structural function and manufacturing process, which is rolling (fragments from the fuselage skin, defined as "plates") or extrusion (fragments from the support structure, defined as "stringers"). Hereafter this aircraft is referred as to "P", with letters in brackets indicating plates (p) and stringers (s). Table 1 summarizes the main features and sample codes of the investigated fragments.

Breguet 765 Sahara
Samples from a double-decker Breguet 765 Sahara n°504 64-PH (hereinafter referred as to "B") were provided by

Table 1 Summarising scheme of fragments and sample codes of P-47D Thunderbolt (P)

Sample	Macroscopic image	Function	Description
P-1		Fuselage skin + structure	Size (max): 230 mm × 100 mm Weight: 114.04 g P-1(p) plate thickness: 1.27 mm P-1(s) stringer thickness: 2.57 mm Rivets: • Head diameter: 7 mm • Shank diameter: 5 mm • Spacing btw rivets: 33 mm
P-2		Fuselage skin	Size (max): 150 mm × 64 mm Weight: 13.42 g P-2(p) plate thickness: 1.04 mm Rivets: • Head diameter: 8 mm • Shank diameter: 6 mm
P-3		Fuselage skin	Size (max): 100 mm × 60 mm Weight: 22.21 g P-3(p1) plate thickness: 1.0 mm P-3(p2) plate thickness: 2.1 mm Rivets: • Head diameter: 7 mm • Shank diameter: 5 mm • Spacing btw rivets: 32 mm • Spacing btw rows of rivets: 7 mm

The white dashed lines indicate where the pieces were cut for metallographic analysis

Martini *et al. Heritage Science*   (2024) 12:16

Page 4 of 21

the association "*Les Ailes Anciennes de Toulouse*" [28] (France). The airplane was built in 1958 for military use and flew from 1959 to 1969. After this period, it was stored outside for almost 47 years, where it was subjected to several structural damages. During the restoration of the aircraft, some parts were replaced and hence original elements were used for this study. Therefore this aircraft was selected as reference for comparison because of the comparable age, the availability of material and the data already collected in previous characterisation work. In fact, studies carried out by Brunet et al. [27, 28] identified the constituent metallic materials of the 765 Sahara as Al-Cu-Mg belonging to the Duralumin family. In particular, the samples used in the present work (Table 2) were:

- B(p): a rolled plate (fuselage skin). Its composition corresponds to the French classification A-U4G, similar to the modern 2017A.
- B(s): an extruded product used as stringer (support structure). Its composition corresponds to the French classification A-U4G1, comparable to 2024 which is still used for structural parts of modern airplanes.

Modern alloys

As candidate modern reference materials, two different Al-Cu alloys belonging to the 2XXX series (2024 and 2017A) were selected since they were identified as the most similar, in terms of composition or microstructure, to the original alloys used according to extensive characterisation works on historic aircraft [3, 28, 31].

The studied alloys and the codes used to identify them were:

- 2024(p): 2024-T3 rolled plate, 1.0 mm thick, (ALUDIS, Aix-les-Bains France)
- 2024(s): 2024-T3511 extruded stringer, 3.1 mm thick, (ALUDIS, Aix-les-Bains France)
- 2017A(p): 2017A-T4 rolled plate, 1.0 mm thick (Bikar Metalle GmBH, Bad Berleburg Germany)

Temper designation T3 indicates that, after solution heat treatment and quenching, the alloy was cold-worked and naturally aged at room temperature, while T3511 designates an extruded shape which also underwent stress relieving (stretching combined with straightening) before natural ageing. Similarly, T4 indicates that the alloy was not cold-worked after solution heat treatment and directly underwent natural ageing [32].

The composition of the alloys reported in supply certificates is summarised in Table 3; the declared compositions were checked by GD-OES analyses, resulting in good agreement.

Materials characterisation

Each plate and stringer sample was observed in three cross-section planes. The rolling plane including the extrusion direction was named "PL0". When the rolling or extrusion direction was not identifiable, the transverse orthogonal planes were named "PL1" and "PL2". All the samples were then embedded in epoxy resin (Hardrock 554) and polished firstly by SiC papers of decreasing granulometry, from 600 to 1200 grit, and

Table 2 Summarising scheme of fragments and sample codes of Breguet 765 Sahara n°504 64-PH (B)
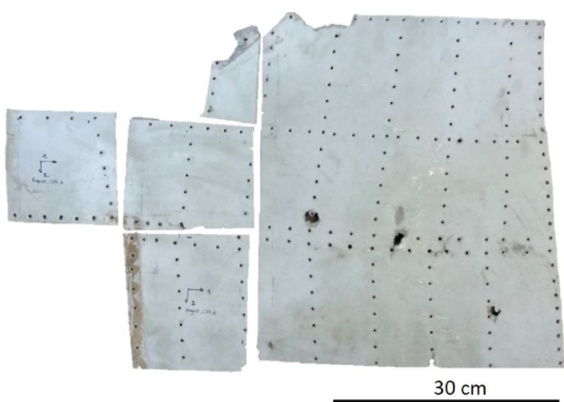
Sample	Macroscopic Image	Function	Description
B(p)		Fuselage skin	Size (max): 900×600 mm Weight: unknown Thickness: 1 mm
B(s)		Stringer	Size (max): 850×50 mm Weight: unknown Thickness: 4 mm

Martini *et al. Heritage Science*   (2024) 12:16

Page 5 of 21

Table 3 Composition of the modern alloys (wt.%), Al to balance, from supply certificates

	Cu	Si	Mg	Mn	Fe	Zn	Ti	Cr	Others
2024	4.3	0.07	1.5	0.52	0.10	0.06	0.04	0.03	0.03
2017A	4.1	0.72	0.74	0.60	0.40	0.18	0.07	0.05	0.05

then on cloths with diamond abrasive paste from 3 μm down to 1 μm. Microhardness measurements ($HV_{0.3}$) were carried out on PL0, PL1 and PL2 sectioning planes of each polished sample by a Galileo Isoscan hardness tester applying a 300 g load for 15 s.The alloy microstructure was observed in polished cross-sections, by optical microscopy (OM) after etching with Keller's solution (1 mL HF, 2.5 mL HNO_3, 1.5 mL HCl in 95 mL deionised water). Grain shape and size were measured by the linear intercept method [29]. Field Emission Gun Scanning Electron Microscope (FEG-SEM, Tescan Mira3) with Energy Dispersive Spectroscopy (EDS, Brucker Quantax 200/30 mm^2) microprobe was used for evaluating the chemical composition of each sample. EDS acquisition was performed on different areas of the metal core in mounted and polished samples, at $500 \times$ magnification (corresponding to areas of about 415×415 μm^2), with a minimum of 5,000,000 counts on each spectrum using the analytical method Phi-Rho-Z without standards, following a standardised calibration method validated on reference samples.

Elemental analysis of the precipitates was carried out by EDS analysis also on coarse intermetallic particles to distinguish between insoluble constituent precipitates and equilibrium precipitates. Image Analysis (IA, ImageJ 1.52a freeware) was used to classify particles with diameters higher than 0.8 μm, from at least 3 backscattered electrons (BSE) images for each investigated cross-section. The main quantitative parameters [30] measured by IA were the following: (i) particle area fraction (%); (ii) circularity ($f_2 = 4\pi \times \frac{[Area]}{[Perimeter]^2}$), which indicates a perfect circle when equal to 1; (iii) Feret diameter *i.e.*, the longest distance between two parallel lines restricting the particle projection perimeter. Coarse particles were then classified as elongated (circularity < 0.8) or rounded (circularity > 0.8) and for each category both the maximum Feret diameter (d_{max}) and the 90th percentile Feret diameter (d_{90}, describing most of the particle population) were measured to quantify particle size.

For P samples, EDS X-ray mapping was performed on cross-sectioned samples to investigate surface modifications (e.g., application of an Al cladding layer) and localised corrosion damage; dispersoids and submicrometric particles were investigated by a Transmission Electron Microscope (TEM, JEOL 2010) operating at 200 kV. Cross-section samples were electrochemically thinned by a Tenupol-5 Struers apparatus operating at 60 V in a solution of methanol and HNO_3 (3:1) at − 15 °C. Precipitates were identified with a CM20 FEG TEM/STEM microscope, operating at 200 kV and chemical elements were identified by EDS (Bruker—Quantax EDS system with silicon drift detector).

Comparison of historic vs. modern alloys: exfoliation and corrosion behaviour
Exfoliation test
The susceptibility to exfoliation of modern and historic aluminium alloys, both plates (2024(p), 2017A(p), P-2(p), B(p)) and stringers (2024(s), P-1(s), B(s)), was assessed by the ASTM G34-01 method for exfoliation corrosion susceptibility (EXCO Test) [26]. This standard test consists in a continuous immersion of test materials in a a 4 M NaCl, 0.5 M KNO_3, and 0.1 M HNO_3 aqueous solution at room temperature. The susceptibility to exfoliation is determined by visual examination through comparison with reference photographs.

Before the beginning of the test, all the specimens (2×2 cm^2) were degreased with acetone, then Kapton tape was used to protect each specimen's back and borders from the test solution. Specimens were then immersed in the solution supported by stick and rods of inert materials and regularly checked after 5, 24, 48, 72 h and at the end of the experiment (96 h), as recommended by ASTM G34-01. Deeper observations of the samples surface and cross-section were carried out by optical and 3D-digital microscopy.

Electrochemical tests
To complete the picture of the corrosion behaviour of modern alloys compared to the historic fragments, electrochemical tests were performed on the following plate and stringer samples:2024(p), 2017A(p), B(p), 2024(s), B(s).

For electrochemical tests, the exposed surface of each sample was cut from the rolling plane or along the extrusion direction. Each specimen was connected to threaded copper wire and then painted and embedded in an epoxy resin to protect the unexposed parts.

Before the electrochemical tests, the exposed surface was polished with emery paper down to 2500 grit and

Martini *et al. Heritage Science*   (2024) 12:16

Page 6 of 21

cleaned with deionized water and ethanol in an ultra-sonic bath.

Electrochemical measurements were carried out in a standard 3-electrode cell with a saturated calomel electrode as a reference and a platinum as a counter-electrode. The potentials are quoted with reference to the calomel scale (E = 0.241 V/NHE).

The evolution of corrosion behavior was monitored, during 7 days of immersion in an aerated aqueous solution of 0.1 M NaCl at 30 °C, by electrochemical impedance spectroscopy (EIS). EIS measurements were performed using the following experimental conditions: polarization (mean square alternating potential signal ± 4 mV) at open circuit potential (E_{oc}); frequency range 100 kHz–1 mHz; 10 frequencies/decade.

For each alloy, cathodic and anodic polarization curves were recorded on separated electrodes at the end of the immersion period (7 days), starting from stable E_{oc}, with a scan rate of 0.2 mV/s.

Localised ageing tests

Experiments to evaluate the role of intermetallic particles in the corrosion of historic and modern alloys were carried out on plate samples P-2(p) and 2024(p), exposed to 0.01 M NaCl aqueous solution for a total time of 19 h, in analogy with previous works [19, 33]. A single drop (about 15 µL) of the NaCl solution was manually deposited every hour on a few square millimetres area of each sample with a 20 µL micro syringe in order to keep the surface continuously wet. To avoid surface drying during night-time, a single-drop automatic dripping system was set up using a peristaltic pump set to minimum speed (0.1 round per minute, corresponding to 1 drop of about 13 µL every 2 min). Micro-scale observations were performed before and after the exposure using a FEG-SEM (Tescan Mira3) with EDS (Brucker Quantax 200/30 mm^2).

Results and discussion

Materials characterisation

All the P fragments displayed several mechanical and structural damages due to the crash event. Moreover, a heterogeneous corrosion layer was detected, particularly on the inner side of the fragments, which was probably left unpainted.

However, the exposure to the clay-rich soil for seven decades, which produced rather stable and adherent soil concretions, helped maintaining an overall good conservation state of the alloy even if some exfoliated areas are present.

On both the internal and external sides of the rolled plates SEM/EDS observation of cross-sectioned samples revealed the presence of the Alclad protective
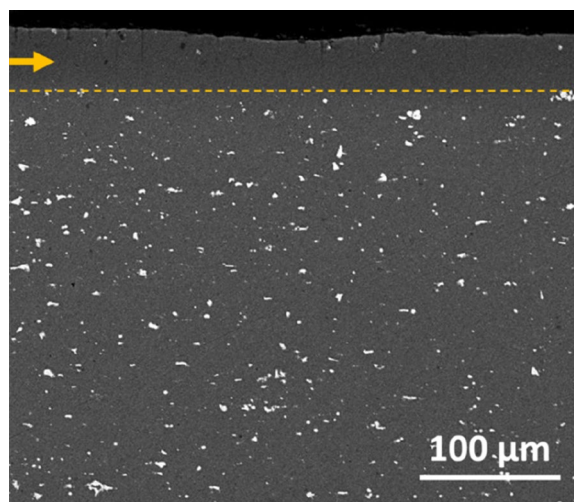

Fig.1 Representative cross-section SEM image showing the presence of Alclad (pure Al layer applied by rolling—top left arrow) onto the surface of P-3(p1) sample

Table 4 Thickness of the Alclad surface layer on the studied P fragments

Sample	Alclad layer thickness, µm	
	Outer	Inner
P-1(p)	64 ± 3	49 ± 2
P-2(p)	30 ± 5	35 ± 5
P-3(p1)	82 ± 2[a] or 40 ± 3[b]	48 ± 2
P-3(p2)	109 ± 2	146 ± 5[a] or 70 ± 10[b]

[a] Non-exfoliated/undamaged areas

[b] Exfoliated/damaged areas

treatment on the alloy (Fig. 1). This treatment consists in the application of a high purity Al sheet onto both sides of the plate by hot rolling. This type of coating was developed by the AlCoA company (USA) in 1927 and frequently applied to aluminium alloys to prevent corrosion [34]. The observed thickness of the Alclad layer ranges from about 30 to 150 µm (Table 4).

Historic alloys were characterised through SEM/EDS analysis to assess the composition (Table 5). EDS analysis of the modern alloys 2024 and 2017A, used to validate the applied SEM/EDS method by comparison with the supplier certificate compositions (Table 3), was also performed and reported in Table 5 for comparison with historic compositions.

The alloy composition for each sectioning plane showed no significant differences as a function of the rolling orientation, so the values were averaged over the three cross-sections for each sample.

Martini *et al. Heritage Science*   (2024) 12:16

Page 7 of 21

Table 5 Elemental composition of P, B, and modern alloy samples measured by EDS analysis (wt.%), averaged over the three cross-sectioning planes

Sample name	Mg	Al	Si	Ti	Cr	Mn	Fe	Ni	Cu	Zn
P-1(p)	1.39±0.02	92.95±0.02	0.14±0.01	0.01±0.00	0.01±0.01	0.49±0.03	0.24±0.04	0.01±0.01	4.69±0.08	0.05±0.01
P-1(s)	1.32±0.06	93.15±0.45	0.18±0.03	0.01±0.01	0.02±0.02	0.55±0.02	0.31±0.01	0.02±0.01	4.33±0.37	0.08±0.01
P-2(p)	1.37±0.02	92.94±0.08	0.09±0.01	0.01±0.01	0.03±0.01	0.51±0.01	0.17±0.01	0.02±0.00	4.75±0.05	0.03±0.01
P-3(p1)	1.47±0.01	92.84±0.08	0.17±0.01	0.01±0.01	0.01±0.01	0.55±0.01	0.28±0.02	0.01±0.00	4.57±0.04	0.04±0.01
P-3(p2)	1.37±0.03	92.78±0.06	0.14±0.02	0.01±0.01	0.01±0.01	0.55±0.02	0.29±0.02	0.02±0.01	4.72±0.04	0.06±0.01
B(p)	0.76±0.02	93.29±0.36	0.59±0.06	0.06±0.03	0.02±0.02	0.70±0.05	0.37±0.06	0.04±0.03	4.14±0.24	0.04±0.03
B(s)	1.46±0.03	92.97±0.21	0.13±0.03	0.03±0.02	0.01±0.01	0.76±0.04	0.18±0.02	0.02±0.02	4.40±0.18	0.04±0.04
2024(p)	1.34±0.00	93.66±0.03	0.03±0.00	0.04±0.01	0.03±0.01	0.44±0.03	0.08±0.01	0.01±0.01	4.24±0.02	0.10±0.02
2024(s)	1.30±0.02	92.78±0.06	0.09±0.00	0.03±0.01	0.01±0.01	0.66±0.01	0.29±0.01	0.01±0.01	4.68±0.06	0.12±0.02
2017A(p)	0.55±0.01	93.76±0.12	0.64±0.04	0.03±0.01	0.04±0.01	0.49±0.02	0.30±0.02	0.01±0.01	3.93±0.07	0.20±0.02

The results for P samples from Thunderbolt P-47D well agree with the composition of the 24S alloy for both plates and stringers according to the historic USA designation [35]. Their composition is close to that of the modern 2024 (Al–Cu 4.5%–Mg 1.5%–Mn 0.6%) but contains slightly higher amounts of Si and Fe. Also the composition of the stringer B(s) from the 765 Sahara is similar to 2024. Conversely, the composition of the plate B(p) from the same aircraft is similar to the modern alloy 2017A.

After alloy identification, investigations focused on the microstructure of the alloys directly related to the ancient thermomechanical treatment, which in turn depends on the function of the component in the aircraft. Metallographic observations, discussed here below, aimed at identifying grain shape and size as well as the distribution of the coarse intermetallic particles, since both aspects significantly affect mechanical properties and corrosion behaviour of Al alloys.

Microstructural observations carried out by optical microscopy along the metallurgical sectioning planes (Fig. 2) revealed the typical structures induced by plastic deformation during the manufacturing process (*i.e.*, rolling for plates, extrusion for stringers).

In rolled plates, both in historic aircraft (P and B) and in modern 2017A and 2024 alloys, equiaxed grains were observed in the rolling plane (PL0 (D1, D2)), whilst in the other planes grains were typically elongated by plastic flow in the rolling D1 direction. Equiaxed grains in the rolling plane (D1, D2) are most likely due to recrystallization by annealing after cold working. This annealing step was indeed largely employed to remove the hardening effects of cold rolling of plates [35]. Conversely (Fig. 2), elongated grains were observed in all the sectioning planes of the extruded stringers, due to severe plastic deformation induced by indirect compression as the billet is pushed unidirectionally through the die.

The grain size of the historic plate and stringer from the P wreck was generally larger than that of the corresponding modern 2024 products, leading to slightly lower hardness values (Table 6). The stringer from the B wreck exhibits very elongated grains (with high aspect ratios) resulting from the severe plastic deformation occurring during the extrusion process. Consequently, this work-hardening effect translates into a higher hardness (152±1). The B plate has a lower hardness (130±2), related to the type of alloy (i.e., Duralumin).

Coarse intermetallic particles (IMPs) were documented by backscattered electron (BSE) images in all planes for each product type (plate or stringer) from the P and the B wreck as well as for modern alloys (Fig. 3). The corresponding quantitative information derived by image analysis is reported in Table 6. The distribution of coarse intermetallics (brighter particles over the dark grey Al-rich matrix in BSE images of Fig. 4) is closely related to the plastic flow induced by manufacturing procedures, such as rolling (for plates) and extrusion (for stringers), as previously discussed for grain size and shape. Data in Table 6 show that the extruded products with comparable composition (historic P-1(s) and modern 2024(s)) displayed coarser particles with a less homogeneous distribution than the corresponding rolled products. By comparison, in the rolling PL0 and PL2 planes of both the ancient and modern stringers, intermetallic particles were preferentially arranged in elongated streaks. However, in the historic stringer, intermetallics showed an average size (Feret diameters d_{max} and d_{90} in Table 6) slightly higher than in the modern stringer.

Intermetallics in Al alloys can be classified in three broad classes [33]: (i) dispersoids (<1 μm in size, forming in the melt for grain refinement); (ii) constituent particles (>1 μm in size, with compositions including transition metals and high melting point, hence not prone to dissolve or respond to thermomechanical processing; they
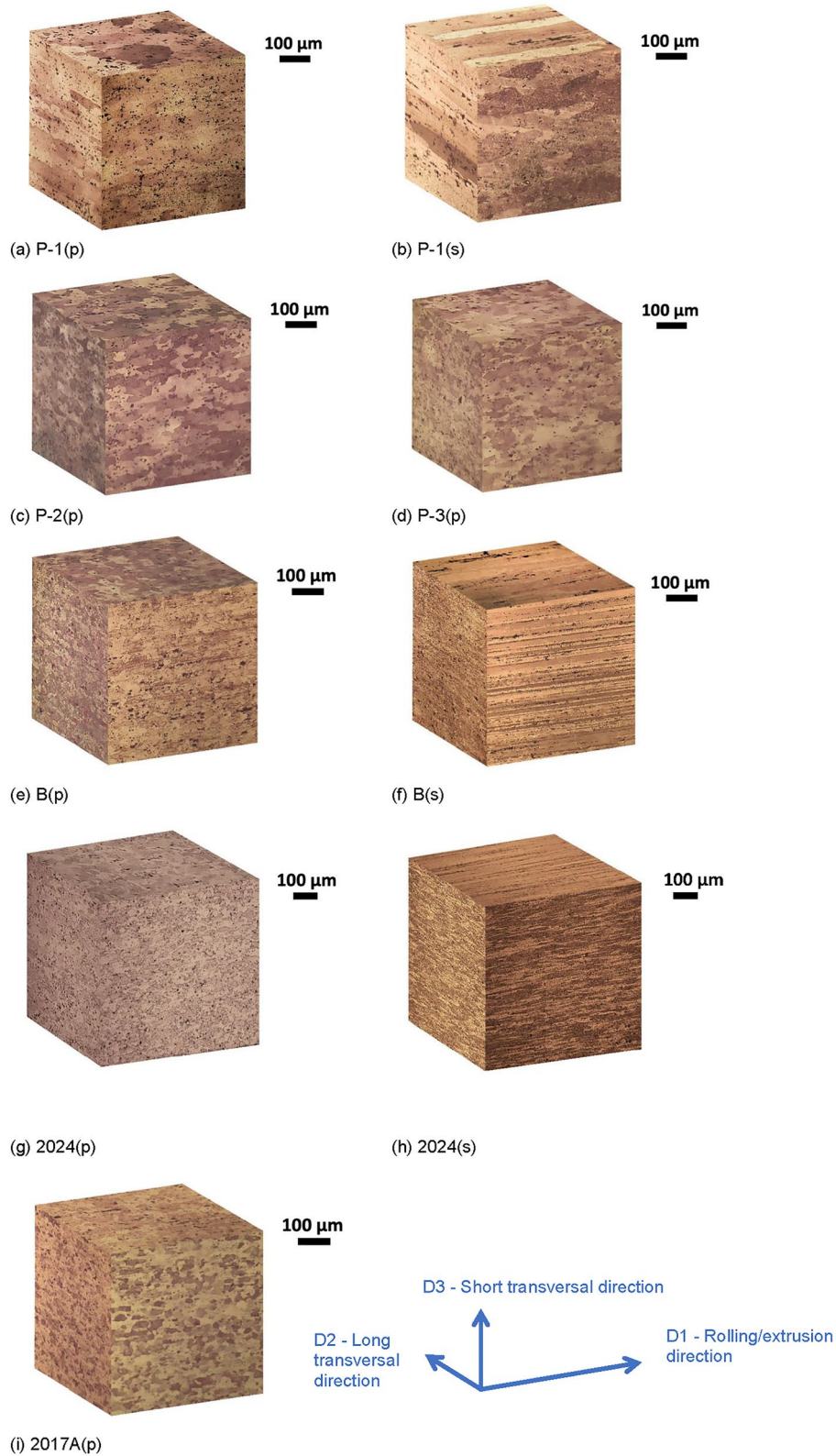
Fig. 2 Isometric representation (optical micrographs in bright field, etching with Keller's reagent) showing grain size and shape of samples from the P (**a–d**) and the B (**e–f**) wrecks, as well as from modern alloys 2024 (**g–h**) and 2017A (**i**). The rolling plane of plates PL0 (D1, D2) is on top of each isometric representation. Extrusion plane for stringers: PL0 (D1, D2). Transverse plane: PL1 (D1, D3)

Martini *et al. Heritage Science*   (2024) 12:16

Page 9 of 21

Table 6 Vickers microhardness (HV$_{0.3}$) and microstructural features measured by image analysis: for coarse IMPs, maximum Feret diameter (d$_{max}$) and 90th percentile Feret diameter (d$_{90}$) are reported both for elongated (with circularity f$_2$ < 0.8) and rounded (f$_2$ < 0.8) particles

| Sample | HV$_{0.3}$ | Plane | Grain size, μm | | | Coarse Intermetallics | | | | | |
| | | | Length (L) | Width (W) | L/W | Area % | Density (IMPs/mm^2) | Circularity < 0.8 (elongated) | | Circularity ≥ 0.8 (rounded) | |
								d$_{max}$ μm	d$_{90}$ μm	d$_{max}$ μm	d$_{90}$ μm
P											
P-1(p)	136±8	PL0	222±89	116±36	1.9	2.2±0.5	5479±1228	18±2	10.0±0.4	7.5±1.3	3.4±0.2
		PL1	186±59	56±14	3.3	2.3±0.2	8192±393	22±2	8.9±0.5	7.0±1.4	2.9±0.1
		PL2	409±24	43±3	9.5	2.3±0.1	6489±603	17±2	8.8±0.9	6.7±0.9	3.4±0.2
P-1(s)	138±10	PL0	206±17	67±15	3.1	3.1±1.2	5522±916	31±7	14.0±5.0	8.0±2.0	2.8±0.6
		PL1	186±8	78±6	2.4	2.5±0.1	7407±206	27±2	10.2±0.6	6.1±0.2	2.9±0.1
		PL2	209±38	60±6	3.5	2.3±0.3	6252±627	28±3	10.4±0.2	7.1±0.9	2.7±0.2
P-2(p)	140±10	PL0	80±13	66±2	1.2	2.1±0.1	5600±286	16±4	6.9±0.4	5.3±0.7	3.1±0.1
		PL1	131±29	56±8	2.3	2.1±0.2	6478±352	14±2	7.9±0.5	5.9±0.3	3.3±0.2
		PL2	117±19	46±8	2.5	1.9±0.1	6297±71	14±2	6.9±0.2	7.9±1.5	3.4±0.1
P-3(p)	141±11	PL0	78±24	70±6	1.1	1.9±0.1	4961±743	15±2	9.7±1.0	9.1±0.9	3.3±0.5
		PL1	126±25	33±5	3.8	2.1±0.3	6812±1737	15±2	8.3±0.5	7.0±0.3	3.2±0.3
		PL2	120±15	39±5	3.1	2.1±0.1	6099±1056	16±2	9.4±0.2	6.9±1.4	3.2±0.3
B											
B(p)	130±2	PL0	30±3	26±2	1.1	2.6±0.3	7778±610	17±4	8.0±1.0	5.7±1.1	2.0±0.2
		PL1	46±10	13±1	3.5	2.7±0.2	11872±1113	14±4	6.8±0.5	4.7±0.6	1.9±0.1
		PL2	34±4	14±1	2.4	2.6±0.2	11846±1425	13±2	6.2±0.2	5.1±0.8	2.1±0.1
B(s)	152±1	PL0	216±37	12±1	18.0	2.4±0.1	2479±1615	11±2	3.7±0.2	3.7±0.7	1.9±0.1
		PL1	160±33	10±1	16.0	2.7±0.1	33599±3398	11±1	3.7±0.1	3.3±0.4	1.7±0.1
		PL2	119±19	15±2	7.9	2.7±0.1	3997±3548	8±1	3.8±0.3	3.3±0.3	1.7±0.1
Modern alloys											
2024(p)	147±9	PL0	64±18	67±12	0.9	1.8±0.2	7694±827	22±6	9.1±0.3	6.0±3.0	2.0±0.1
		PL1	121±26	50±7	2.4	1.2±0.2	5380±980	16±3	8.1±0.2	4.8±0.7	2.1±0.3
		PL2	113±12	39±2	2.9	1.2±0.4	3573±1049	24±5	7.8±0.5	5.4±0.6	2.4±0.1
2024(s)	145±16	PL0	144±26	68±21	2.1	1.6±0.3	8606±1478	17±2	5.6±0.4	4.1±0.5	2.2±0.2
		PL1	171±17	19±1	9.0	1.1±0.1	8160±1048	14±1	5.4±0.3	3.8±0.6	2.0±0.1
		PL2	104±116	40±22	2.6	1.1±0.2	8915±1575	10±1	5.0±0.1	3.6±0.1	2.0±0.1
2017A(p)	122±12	PL0	49±11	45±9	1.1	1.9±0.3	7655±118	14±2	7.3±0.1	8.0±1.0	2.8±0.1
		PL1	56±10	33±2	1.7	2.0±0.2	11287±113	16±3	7.1±0.1	8.0±2.0	2.0±0.1
		PL2	88±17	31±2	2.8	2.0±0.1	11951±272	16±3	7.9±0.5	8.0±2.0	2.1±0.2
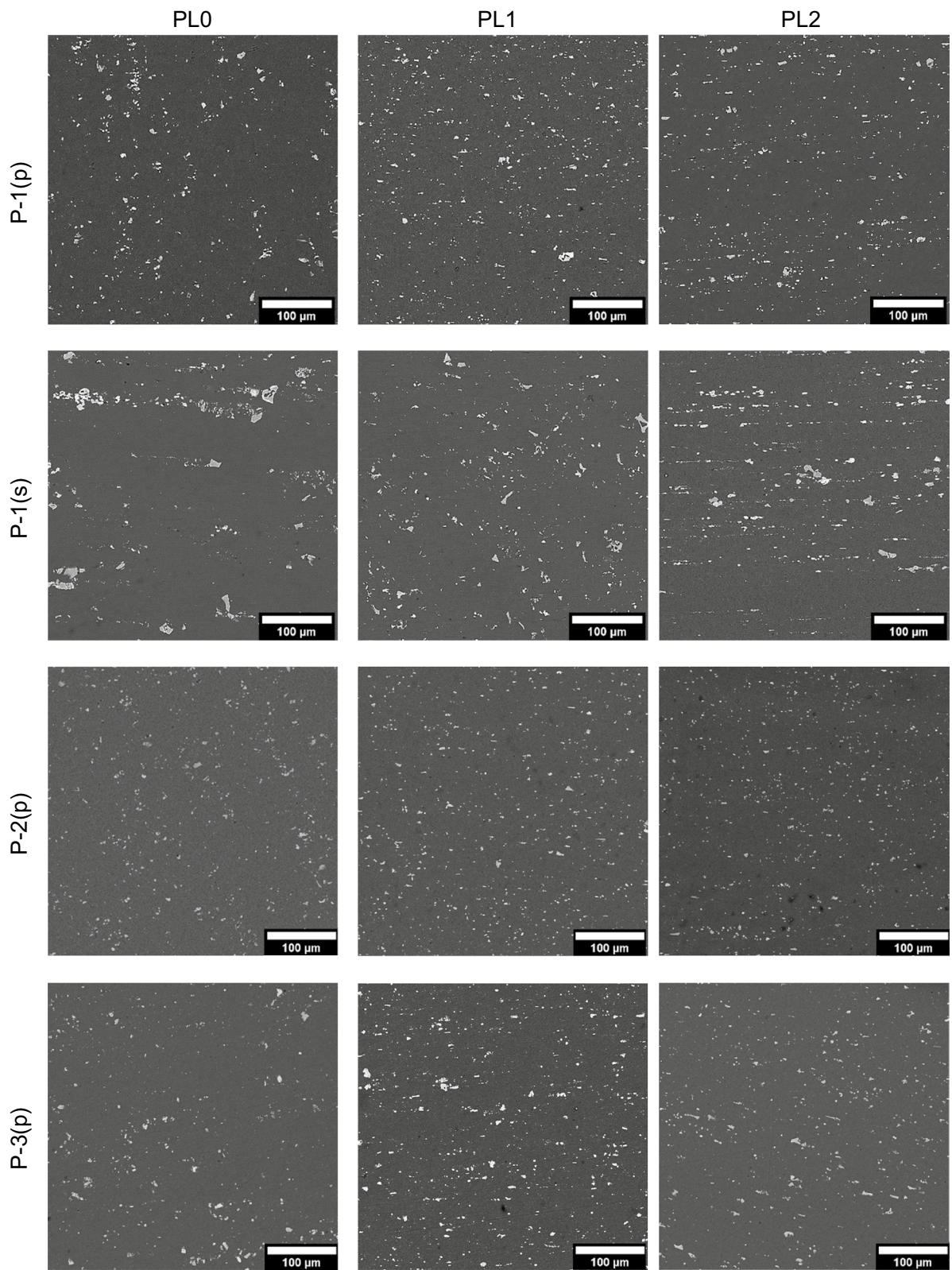
Fig. 3 Backscattered Electron images showing the distribution of coarse intermetallic particles in samples from the P and B wrecks, as well as in modern alloys (2024 and 2017A) along the plane which includes the rolling or extrusion direction (PL0) and the transverse PL1 and PL2 planes
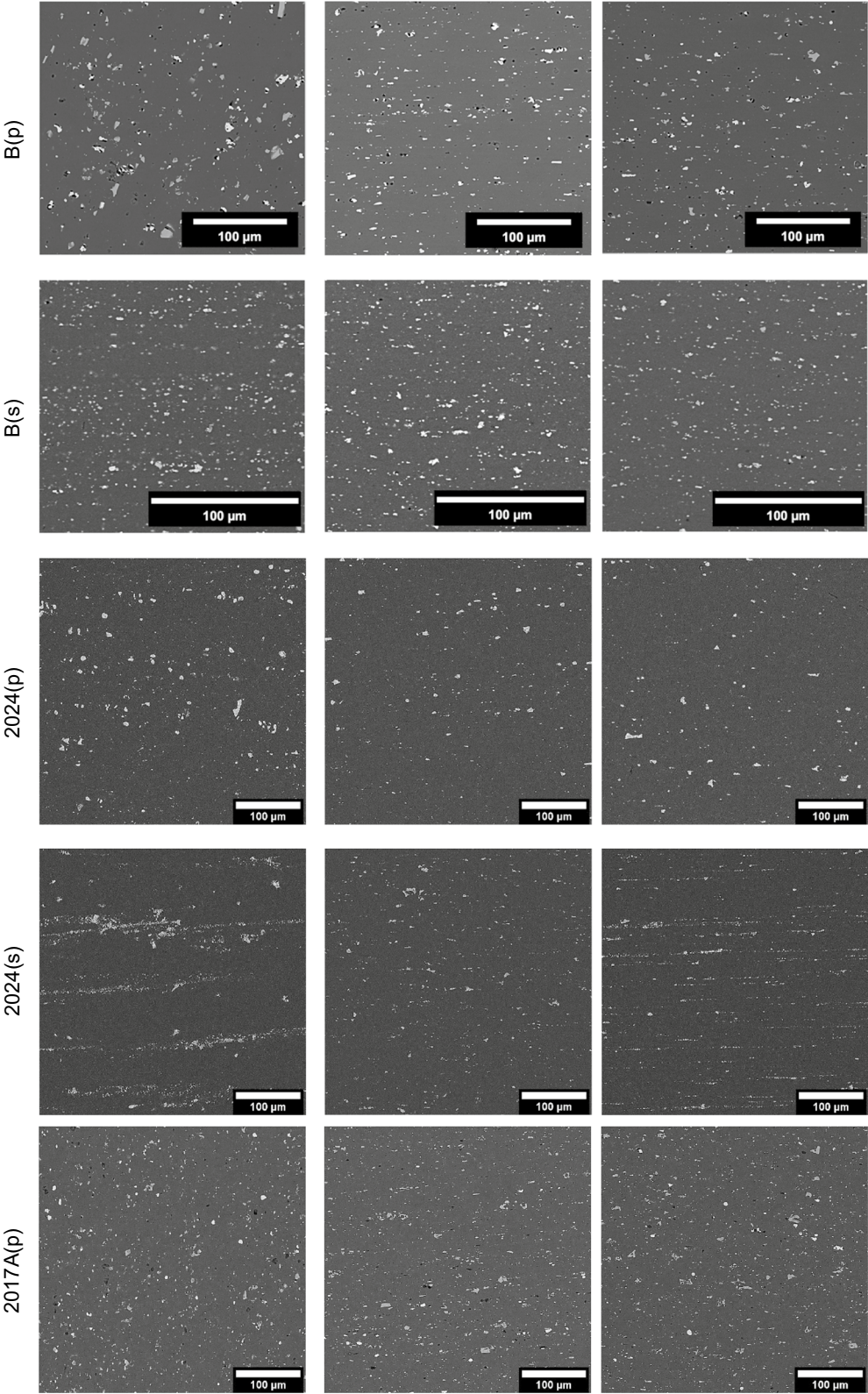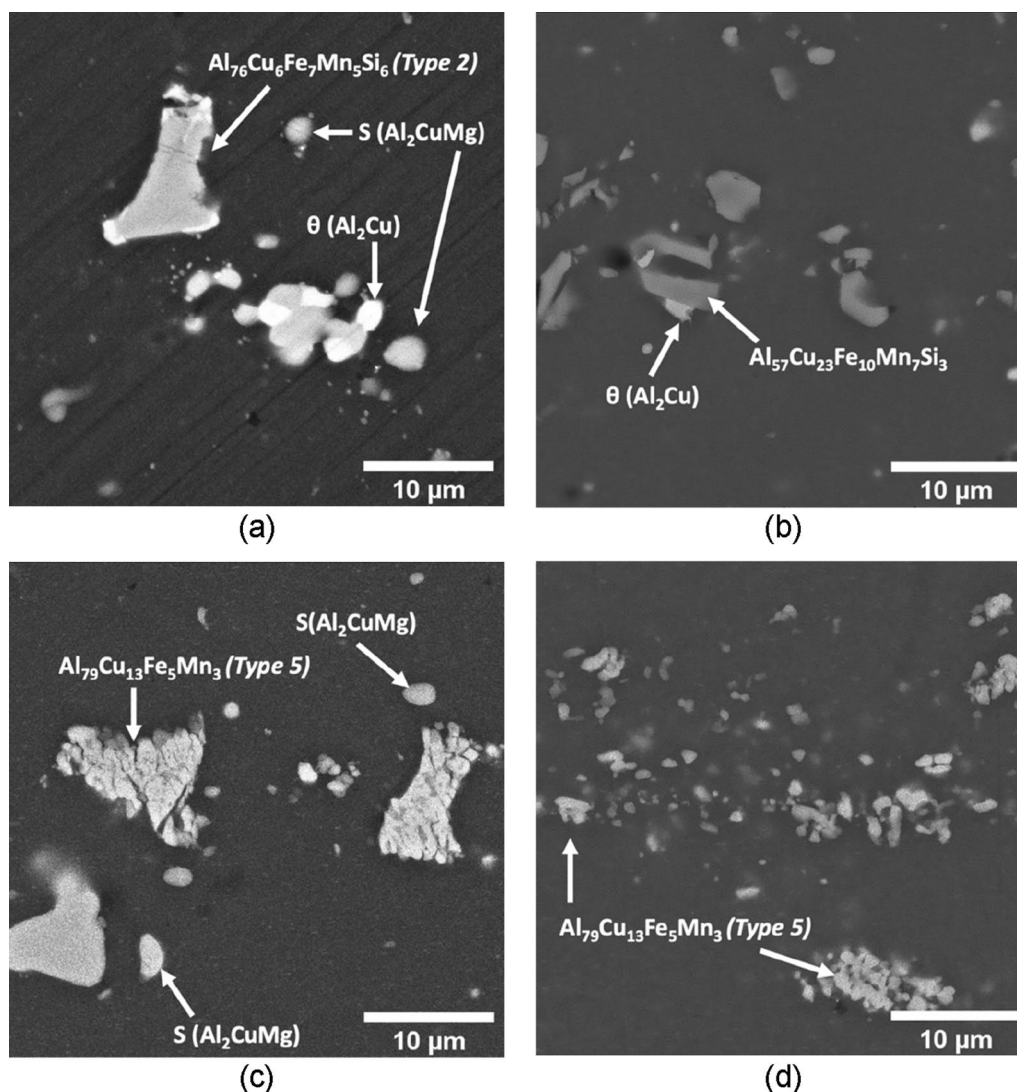
Martini *et al. Heritage Science* (2024) 12:16

Page 11 of 21

Fig. 3 continued

Fig. 4 Backscattered Electron images of coarse intermetallic particles in the PL0 plane for: (**a**) 24S historic alloy (P wreck), and in the modern alloys: (**b**) 2017A(p), (**c**) 2024(p), (**d**) 2024(s). Type of particle (for alloys close to 2024) refers to the classification by Birbilis et al. [33]

may undergo redistribution due to mechanical processing such as rolling or extrusion); (iii) precipitates (such as submicrometric θ-Al_2Cu forming during heat treatment in the solid state for age-hardening).

In the samples from the P wreck, both Fe-containing constituent particles (CP) and precipitates such as θ-Al_2Cu and S-Al_2CuMg were detected (Fig. 4), in agreement with observations made on other historic alloys such as A-U4G1 (the French equivalent of the American 24S used for the P aircraft) [31]. Whilst equilibrium phases are relatively small and rounded (particles with circularity ≥ 0.8 showed 90th percentile Feret diameter (d_{90}) ≤ 3 μm, Table 6), CPs are more elongated, angular and larger (particles with circularity < 0.8 showed d_{90}

from about 5 to 10 μm, with maximum Feret diameter (d_{max}) up to about 30 μm). Since the intermetallics mostly affecting localised corrosion are the cathodic Cu-rich CPs, due to both their size range and higher nobility than Al-rich matrix [19, 36], in order to monitor their evolution after localised ageing tests (Sect. "Localised ageing tests") we classified CPs of alloys corresponding to 2024 in three main types, according to Birbilis et al. [33]: (i) type 1 ($Al_{77}Cu_{10}Fe_7Mn_5Si_2$); (ii) type 2 ($Al_{76}Cu_6Fe_7Mn_5Si_6$); (iii) type 5 ($Al_{79}Cu_{13}Fe_5Mn_2Mg_{0.7}Si_{0.2}$, interchangeable with Al_7Cu_2Fe). Some representative examples are shown in Fig. 4.

The area % occupied by IMPs (Table 6 and Fig. 5) is generally higher for the historic than for the
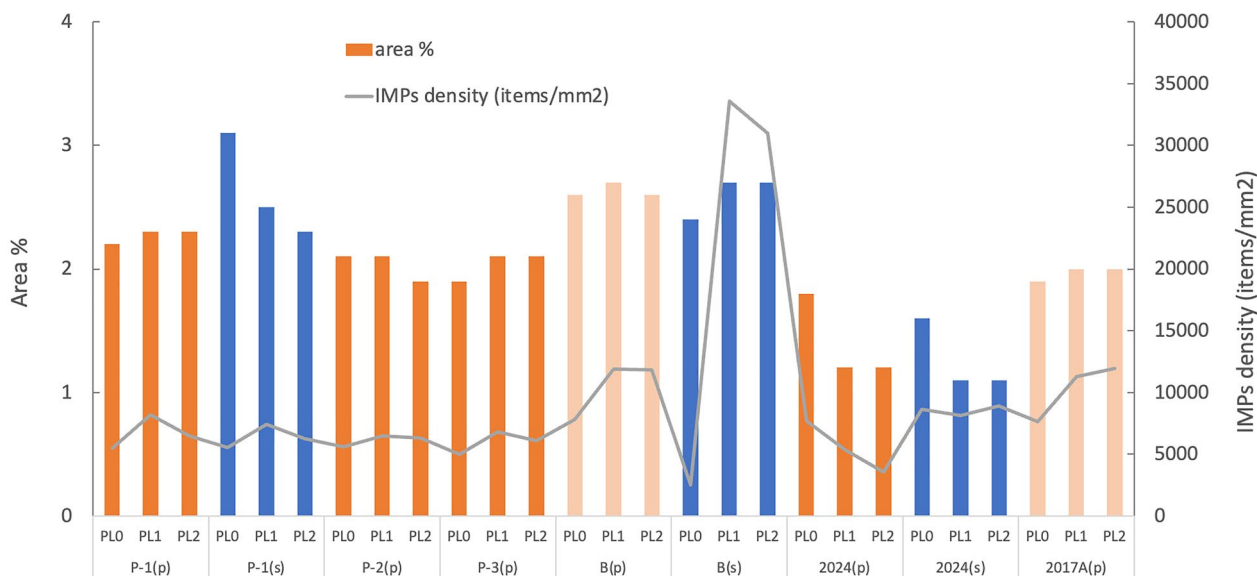
Fig. 5 Intermetallic particles (IMPs) distribution: area % (bars: orange for plates, blue for stringers; Super-Duralumin-type alloys are darker than Duralumin-type ones) and density (grey line)

corresponding modern alloys in each product category (plate and stringer), with higher values for stringers than for plates. The density of IMPs (number of particles per mm^2), which may be related to corrosion behaviour (i.e., the higher the IMP density, the higher the number of potential attack sites [37]), is higher for 2017 (or Duralumin-type alloys: historic B(p), as well as modern 2017A(p)) than for 2024, except for the historic stringer B(s) from the 765 Sahara. However, in all the other cases, where both historic and modern samples are available for comparison, IMP density does not seem to change significantly from historic to modern alloys, due to the tendentially higher size of IMPs in historic alloys (d_{90} and d_{max} in Table 6).

TEM observations were performed on samples P-1(p), P-2(p) and P-1(s) from the P wreck (Fig. 6), showing the presence of dispersoids *i.e.*, Mn-rich particles with a diameter ranging from tens to few hundreds of nanometres. The role of these dispersoids is to control grain size and resistance to re-crystallization [28, 31]. Nanoscale hardening precipitates inside the matrix (which impede the motion of dislocations, increasing mechanical strength) are not observable at this scale. It indicates a T3 or T4 temper for both the plates and the stringer, with no significant difference between the rolled and extruded products, similarly to what found for the alloys of the B wreck [28].

The stoichiometry and morphology of the constituent particles is of major concern for a deep understanding of the material behaviour, since, as previously said, these particles play a key role in localised corrosion phenomena which often occur in Al alloys.

The morphology of localised corrosion is highlighted in Fig. 7a–d, which shows EDS X-ray maps of cross-sectioned samples. The rolled products present different degrees of pitting, characterised by marked dissolution of
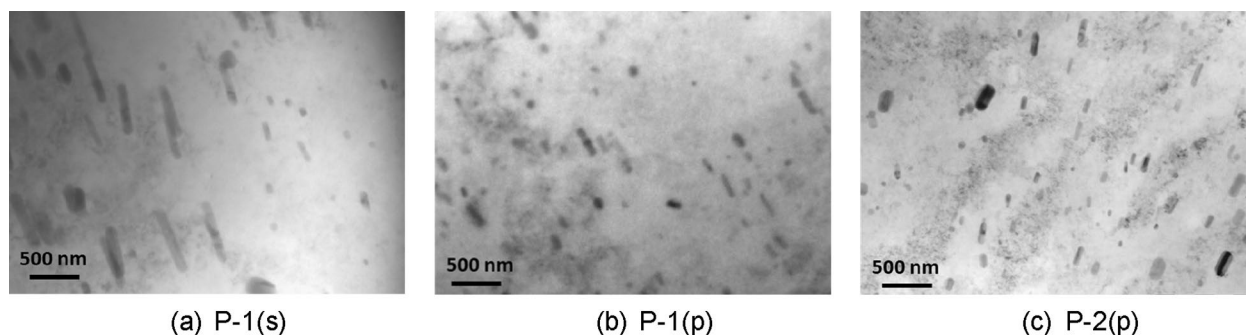

(a) P-1(s) (b) P-1(p) (c) P-2(p)

Fig. 6 TEM images (in bright field) of samples from the P wreck, showing the Mn-rich dispersoids
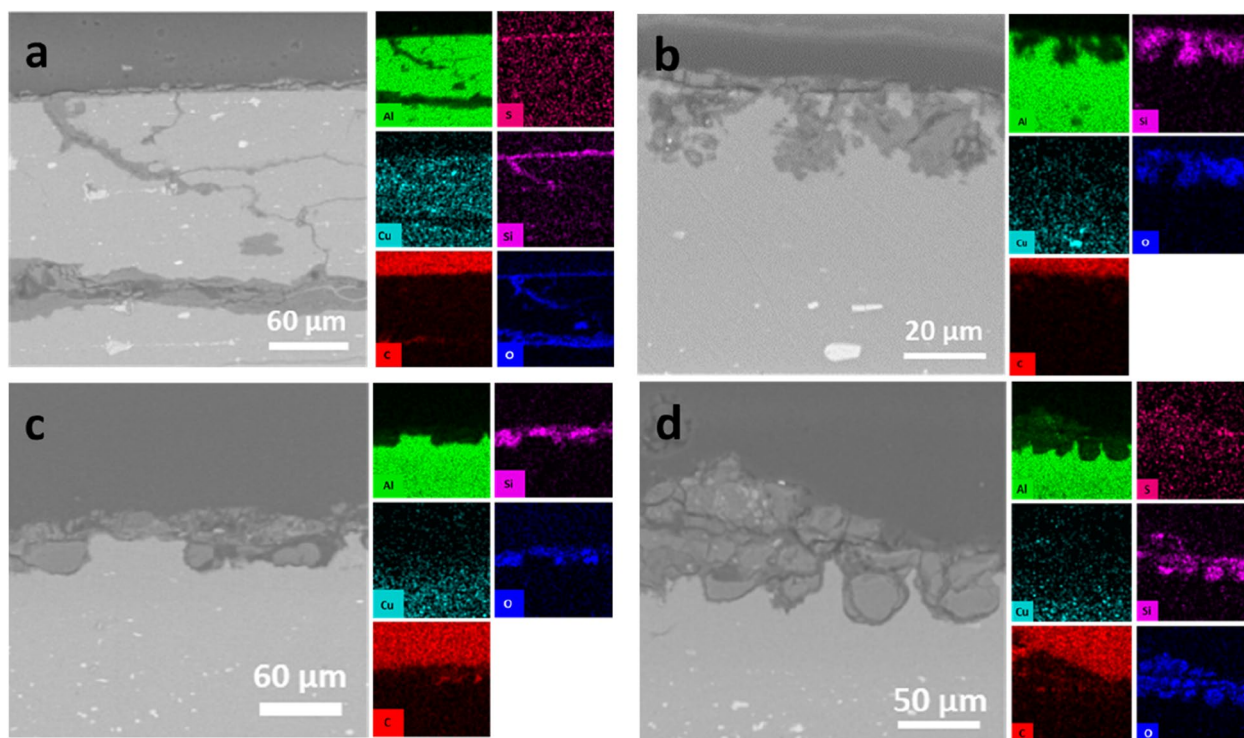
Fig. 7 BSE-SEM images and EDS X-ray maps of the cross-sectioned samples from the P wreck: (**a**) P-1(s), (**b**) P-1(p), (**c**) P-2(p) and (**d**) P-3(p)

the Al element in the corrosion layer (Fig. 7b–d), whilst the extruded one (Fig. 7a) is more subjected to exfoliation phenomena, which are correlated with the elongated grain structure (Fig. 2) as well as with the preferential distribution of intermetallic particles in the plastic flow direction (Fig. 3). The systematic presence of the Si and O elements in the corrosion layer, as well as S in some cases, is linked to burial in clay-based soil. It has to be noticed also that Cl element was not detected by EDS and is therefore not mentioned here.

Corrosion behaviour of historic vs modern alloys
Exfoliation test
EXCO test was performed on historic alloys both from P and B aircraft, as well as on 2017A and 2024 modern alloys, to compare their susceptibility to exfoliation.

As recommended by ASTM G34 [26], since none of the specimens reached the maximum exfoliation level before the end of the test, after 96 h of exposure all the samples were extracted from the test solution, dried and photographed for comparison with the reference images. Visual observation, combined with 3D digital microscopy images taken on the surface of samples (dried after EXCO) and optical images of cross-sections (Fig. 8), allowed to classify the degree of exfoliation of historic and modern samples.

The comparison of corrosion morphologies after EXCO tests showed that both historic stringers are very susceptible to exfoliation, with the B(s) stringer showing extensive exfoliation (ED class) in agreement with the previously discussed high IMPs density and grain structure. The P-1(s) stringer displays a comparable behaviour to the corresponding modern alloy (2024), as expected on the basis of microstructural data. Also in the case of the P-2(p) plate (again analogous to 2024), a comparable behaviour was observed for the historic and the modern sample, both moderately susceptible to exfoliation. Conversely, the Duralumin historic B(p) plate (analogous to 2017A), is susceptible to exfoliation whilst the modern alloy 2017A(p) undergoes localised corrosion with crater-like morphologies; the higher susceptibility to exfoliation of the B plate may be related with its slightly finer and more elongated grain structure (Fig. 2 and Table 6) than the modern 2017A plate. In fact, exfoliation is reported to predominantly occur in products with markedly directional structures [15].

In order to have a clearer picture of the corrosion behaviour of both historic and modern alloys, electrochemical tests were carried out after EXCO, specifically focusing on the discrepancies between the historic B plate and the modern 2017A alloy.
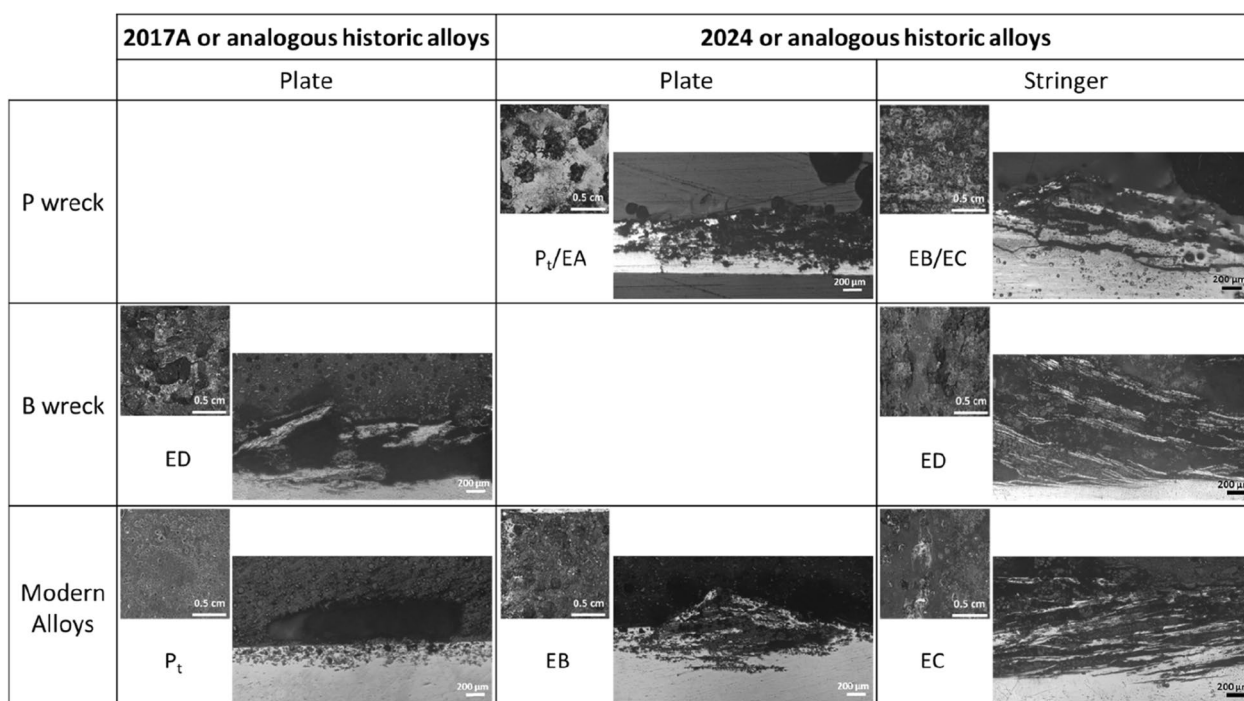
Martini *et al. Heritage Science*   (2024) 12:16

Page 15 of 21

Fig. 8 Optical macrographs of the exposed surface and cross-section images of exfoliated samples after EXCO test (96 h). Under the macrographs is indicated the degree of exfoliation following the classification provided by ASTM G34 (P_t = pitting; EA = superficial exfoliation; EB = moderate exfoliation; EC = severe exfoliation; ED = very severe exfoliation)

Electrochemical tests

Electrochemical tests were conducted to compare the corrosion behaviour of the plates and stringers of the historic B wreck with that of their corresponding modern alloys, namely 2017A and 2024. The evolution of corrosion processes was studied by monitoring the time trends of the polarization resistance (R_p), estimated form EIS spectra, and the corrosion potential (E_{cor}) values during 7 days of immersion in NaCl 0.1 M (Fig. 9).

During the first immersion days the R_p values of both historic and modern rolled alloys rapidly increased from about 10 to 61 kΩ.cm^2 for 2017A(p) and to about 50 kΩ.cm^2 for B(p) and 2024(p). Then, during the exposure, R_p of all alloys slightly decreased and settled, at the end of the test, at values close to 22, 27 and 34 kΩ.cm^2, for B(p), 2017A(p) and 2024(p) respectively (Fig. 9A). The corresponding E_{cor} values (Fig. 9B) decreased during the first immersion period (1–3 days), due to the dissolution of the naturally formed passive layer followed by the precipitation of corrosion products that slowed down the cathodic process. After 7 days, values around -730 ± 20 mV/SCE were achieved by both modern and historic rolled alloys.

For modern and historic extruded alloys, similar R_p and E_{cor} trends were found (Fig. 9C, D). In fact, also for extruded alloys, a rapid increase in polarization

resistance was observed at short exposure times; this increase was more pronounced in the case of alloy 2024(s), but at the end of the exposure both modern and historic alloys reached values around 34 kΩ.cm^2, similar to those measured at the same immersion time on the rolled alloys. During the first immersion period a more marked decrease of E_{cor} values was observed for the historic stringer B(s) (Fig. 9D), but quite close final E_{cor} values, around -750 $\pm$ 20 mV/SCE, were achieved by both alloys at the end of exposure (Fig. 9D).

The polarisation curves collected at the end of exposure in 0.1 M NaCl, on both the rolled and extruded alloys (modern and historic) are shown in Fig. 10 A and B respectively, and the corresponding corrosion potential (E_{cor}), corrosion current (i_{cor}) and breakdown potential (E_{BD}) values are collected in Table 7.

After 7 days of immersion, the polarisation curves of all the samples showed a pseudo-passive behaviour, probably related to the precipitation of corrosion products which form a fairly protective film on the electrode surface.

This agrees with the impedance measurements that showed a progressive increase in polarisation resistance and a decrease in corrosion potential. Probably at short exposure times when high corrosion potentials were measured, the materials were in an active condition,
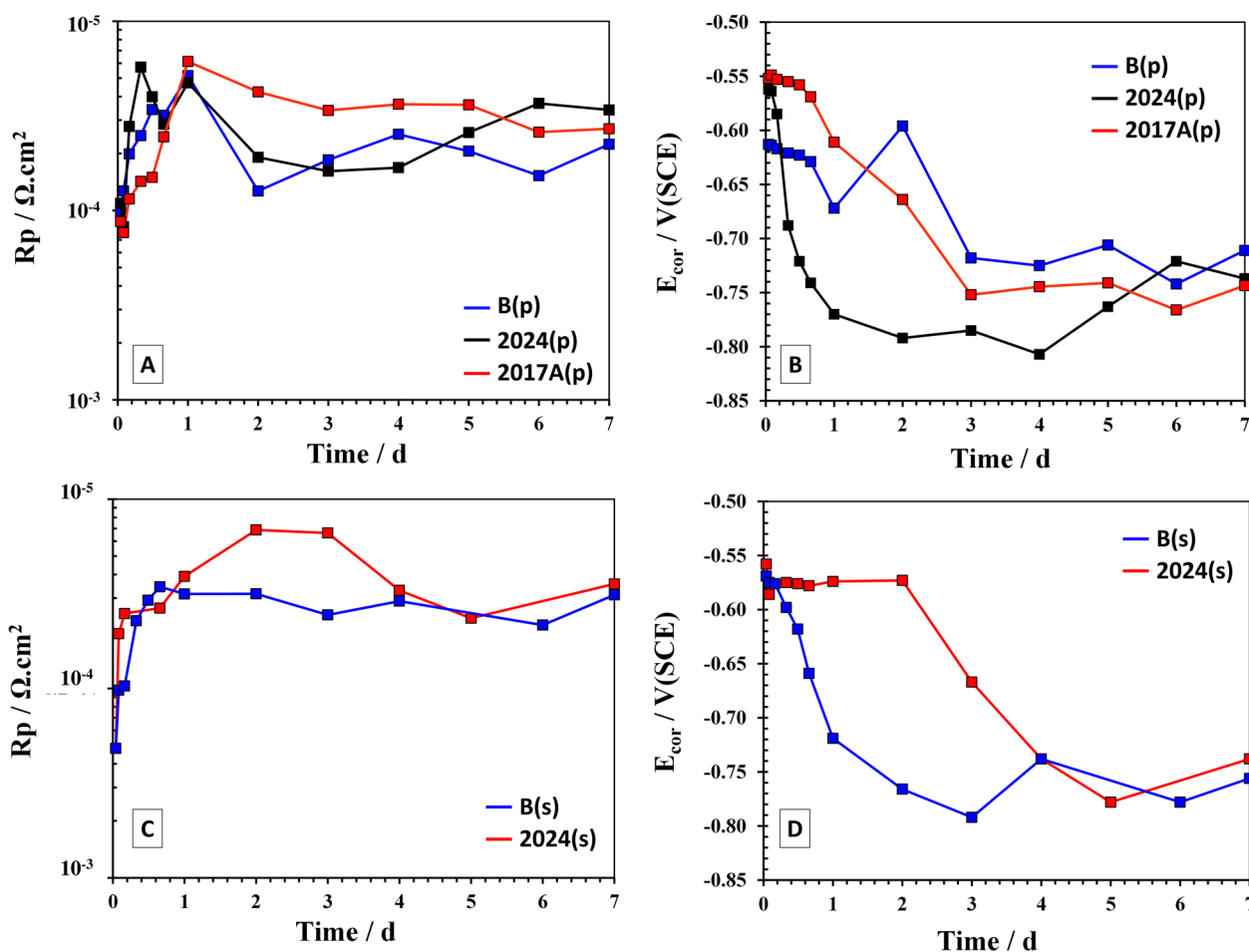
Fig. 9 R_p and E_{cor} values recorded during 7 days of exposure to NaCl 0.1 M: **A**, **B** modern and historic rolled alloys (p: plate); **C**, **D** modern and historic extruded alloys (s: stringer)

stimulated by the strong cathodic activity of the surface-exposed Cu-rich intermetallics. However, as the exposure time increased, the precipitation of a layer of corrosion products induced the formation of a pseudopassive film which slowed down the cathodic process, lowering the corrosion potential and reducing the corrosion currents to values between 1.43 and 2.34×10^{-6} A/cm^2 (Table 7).

The materials tested showed very similar polarisation behaviour, in fact quite similar corrosion and passive currents were observed. Only small differences in the breakdown potential (E_{BD}) were detected: E_{BD} was slightly higher for the modern rolled alloys ($E_{BD} = -0.524$ and -0.550 V for 2017A(p) and 2024(p), respectively) than for the historic B(p) alloy ($E_{BD} = -0.592$ V for B(p)), suggesting a slightly higher susceptibility to localised corrosion of the historic alloy compared to the modern one, in agreement with the results of the EXCO test.

However, based on all the tests performed, the corrosion behaviour of modern alloys for both stringer and plate samples was comparable with that of historic alloys, in agreement with microstructural data. The results obtained proved that, even though 2017A rolled plates in EXCO tests showed a different corrosion morphology in comparison to the corresponding historic alloy (*i.e.*, no exfoliation), from an electrochemical point of view they exhibited a comparable corrosion behaviour. Therefore, also modern 2017A rolled plates could be used as an analogous metal substrate, ideally well suited for electrochemical screening of protective treatments and coatings on historic aircraft.

Localised ageing tests
To better understand corrosion phenomena induced by intermetallic particles, the historic alloy 24S from P (P-2(p)) and the modern 2024(p) were locally exposed to a 0.01 M NaCl solution for a total time of 19 h, as described in Sect. "Localised ageing tests".
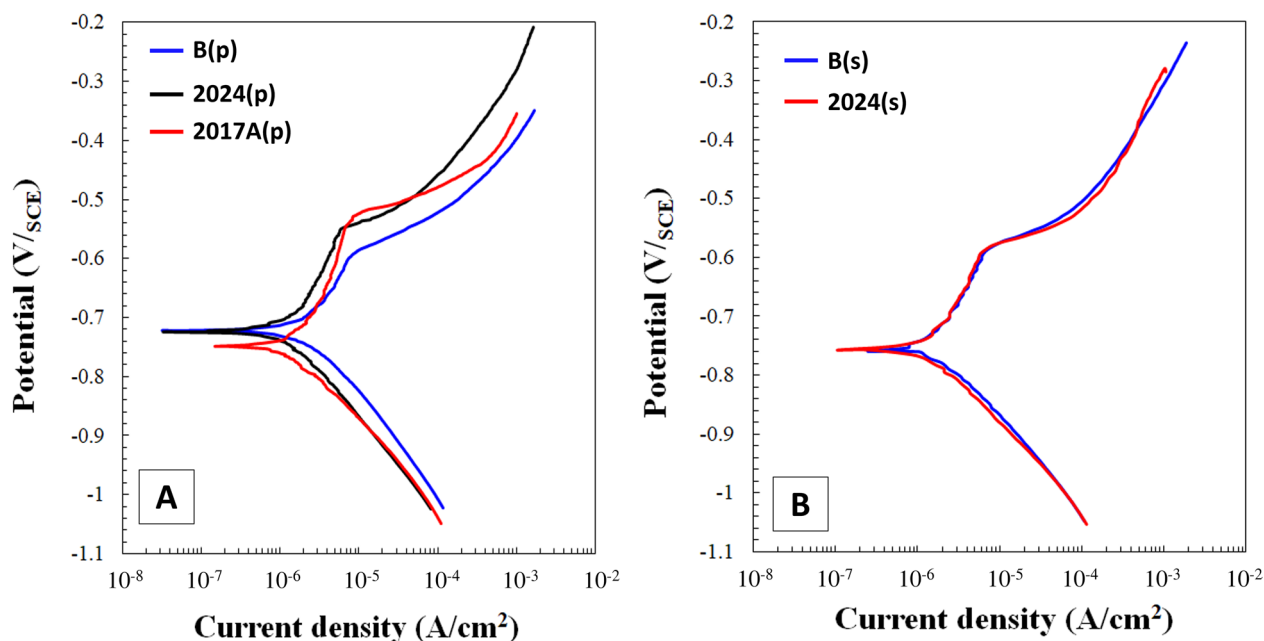
Fig. 10 Potentiodynamic polarization curves recorded after 7 days of in immersion in NaCl 0.1 M: modern and historic **A** rolled and **B** extruded alloys

Table 7 E_{cor} and i_{cor} values evaluated from potentiodynamic polarizations curves after 7 days of immersion in NaCl 0.1M

		E_{cor} (mV/SCE)	J_{cor} (A/cm^2)	E_{BD} (mV/SCE)
Rolled	B(p)	-0.722	2.34×10^{-6}	-0.592
	2024(p)	-0.722	1.44×10^{-6}	-0.550
	2017A(p)	-0.75	1.46×10^{-6}	-0.524
Extruded	B(s)	-0.757	1.43×10^{-6}	-0.584
	2024(s)	-0.757	1.43×10^{-6}	-0.584

The observations were made on selected particles according to their morphology and chemical composition before and after 19 h of immersion. The results are summarised in Figs. 11, 12, 13, 14.

In general, as expected, different behaviour was shown by intermetallic phases of different composition. In the case of the historic alloy, the ($Al_{77}Cu_{10}Fe_7Mn_5Si_2$) type 1 particle (Sect. "Materials characterisation") doesn't exhibit evidence of corrosion attack from a morphological point of view. EDS data show a slight depletion of Si element (Fig. 11a). These types of IMPs were subject to little or no selective attack and remained unaffected during exposure. Although these IMPs tended to behave cathodically with respect to the aluminium matrix, the slow kinetics of the oxygen reduction process on these intermetallics made the corrosive attack on the surrounding matrix much less severe than that observed around other Cu-rich intermetallics [38, 39]. Conversely,

for type S (Al_2CuMg), the formation of a deep trench was observed, associated with a strong loss of Al as well as a relative strong enrichment in Cu and, less markedly, in Mg and Fe (Fig. 11b). In addition, some composite particles forming globular aggregations of Cu were observed (Fig. 12). These Cu aggregates are probably due Cu redeposition as already observed by Kosari et al. [19].

For the modern 2024 alloy, analogous and more clear results were obtained in terms of localised attack triggered by intermetallic particles, as shown by the example in Fig. 13 of relative Cu enrichment as well as local matrix dissolution around a type S particle. This is due to localised matrix dissolution around the partially corroded particle, involving a two-step process. Initially, due to the presence of Mg, the S-phase has an anodic open circuit potential (OCP) with respect to the matrix and underwent selective dissolution of Al, resulting in Cu enrichment. In a second step, under these new conditions, the polarity of the now Cu-rich intermetallic reversed and became highly cathodically active, inducing the dissolution of the Al matrix at the interface and causing partial trenching.

Type S particles behave as an active phase undergoing local degradation over a very short time-scale [19]. The elemental variations both in the particle and in the surrounding matrix composition are pointed out by the EDS line profiles (Fig. 14). The X-ray intensity profiles measured along a line crossing both the IMP and the surrounding matrix showed that during the exposure the
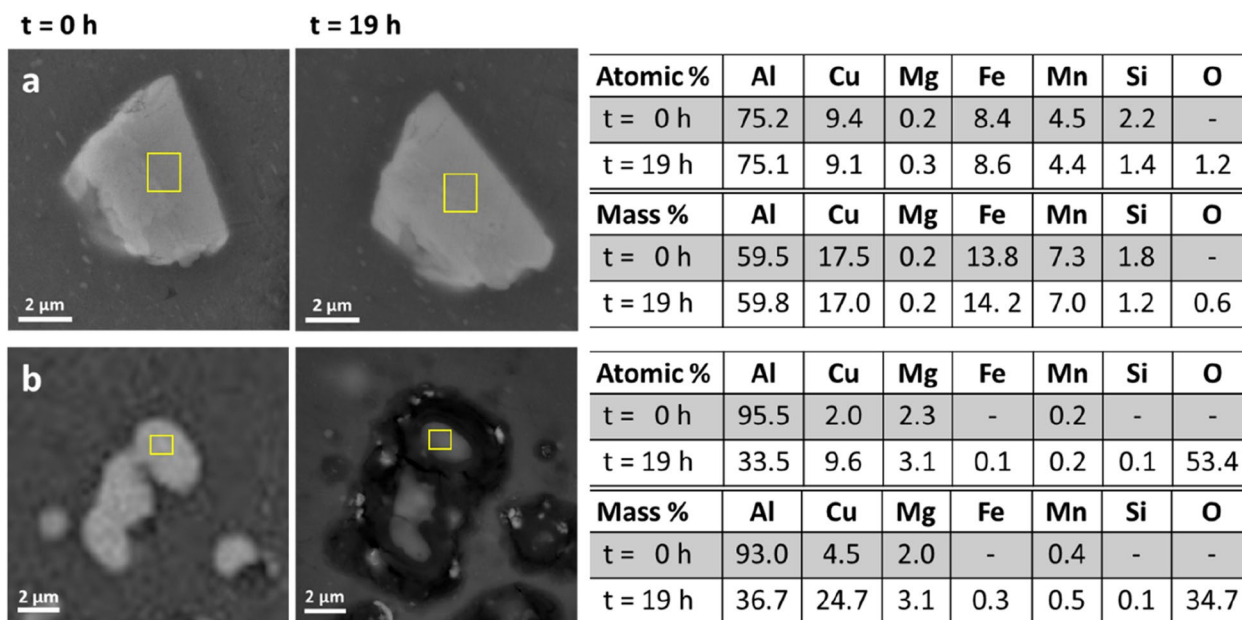
Martini *et al. Heritage Science*   (2024) 12:16

Page 18 of 21

Atomic %	Al	Cu	Mg	Fe	Mn	Si	O
t = 0 h	75.2	9.4	0.2	8.4	4.5	2.2	-
t = 19 h	75.1	9.1	0.3	8.6	4.4	1.4	1.2
Mass %	Al	Cu	Mg	Fe	Mn	Si	O
t = 0 h	59.5	17.5	0.2	13.8	7.3	1.8	-
t = 19 h	59.8	17.0	0.2	14. 2	7.0	1.2	0.6

Atomic %	Al	Cu	Mg	Fe	Mn	Si	O
t = 0 h	95.5	2.0	2.3	-	0.2	-	-
t = 19 h	33.5	9.6	3.1	0.1	0.2	0.1	53.4
Mass %	Al	Cu	Mg	Fe	Mn	Si	O
t = 0 h	93.0	4.5	2.0	-	0.4	-	-
t = 19 h	36.7	24.7	3.1	0.3	0.5	0.1	34.7

Fig. 11 Historic P-2(p) sample—SEM images and EDS data of (**a**) type 1 particle (according to Birbilis et al.[33]), (**b**) type S particle (Al_2CuMg), before (t = 0 h) and fter localised ageing (t = 19 h) in 0.01 M NaCl solution

Atomic %	Al	Cu	Mg	Fe	Mn	O
1 (matrix)	73.8	2.0	0.7	0.1	0.2	23.2
2 (IMP)	62.2	10.5	0.7	1.1	0.2	25.3
3 (Cu glob.)	66.9	13.4	0.8	0.1	0.3	18.4
Mass%	Al	Cu	Mg	Fe	Mn	O
1 (matrix)	78.9	5.0	0.7	0.2	0.5	14.7
2 (IMP)	59.1	23.4	0.6	2.2	0.5	14.2
3 (Cu glob.)	60.3	28.5	0.6	0.3	0.5	9.8
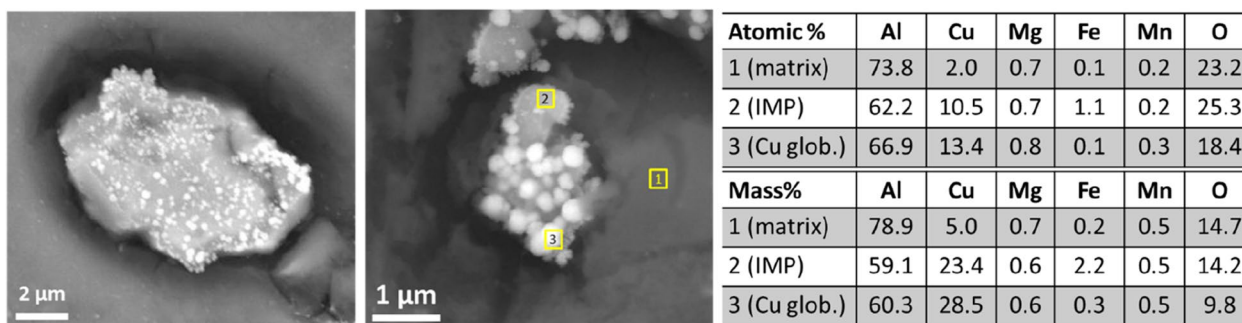
Fig. 12 Historic P-2(p) sample—SEM images of intermetallic particles (IMPs) with globular Cu aggregations, taken after localised ageing (t = 19h, 0.01 M NaCl solution). Localised EDS data comparing the elemental composition of the Al-rich matrix (1), IMP (2) and Cu globular aggregates (3) in the right-hand image
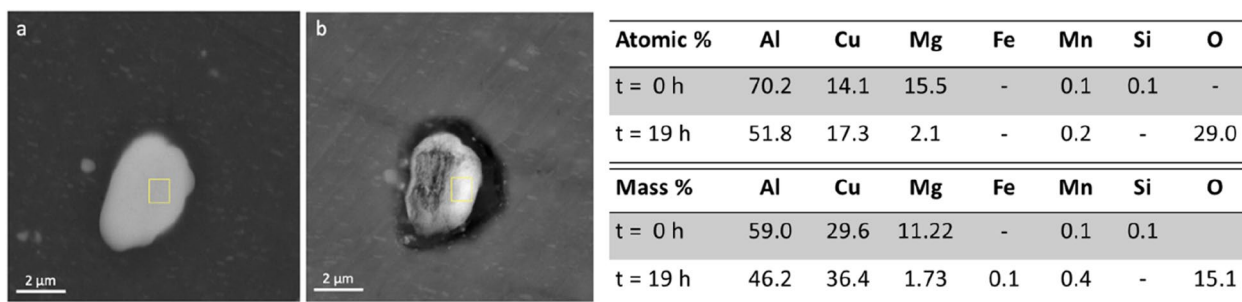

Atomic %	Al	Cu	Mg	Fe	Mn	Si	O
t = 0 h	70.2	14.1	15.5	-	0.1	0.1	-
t = 19 h	51.8	17.3	2.1	-	0.2	-	29.0
Mass %	Al	Cu	Mg	Fe	Mn	Si	O
t = 0 h	59.0	29.6	11.22	-	0.1	0.1	
t = 19 h	46.2	36.4	1.73	0.1	0.4	-	15.1

Fig.13 Modern reference alloy 2024(p)—SEM image and EDS elemental map taken on a type S particle (Al_2CuMg) **a** before and **b** after localised ageing (19 h, 0.01 M NaCl solution)
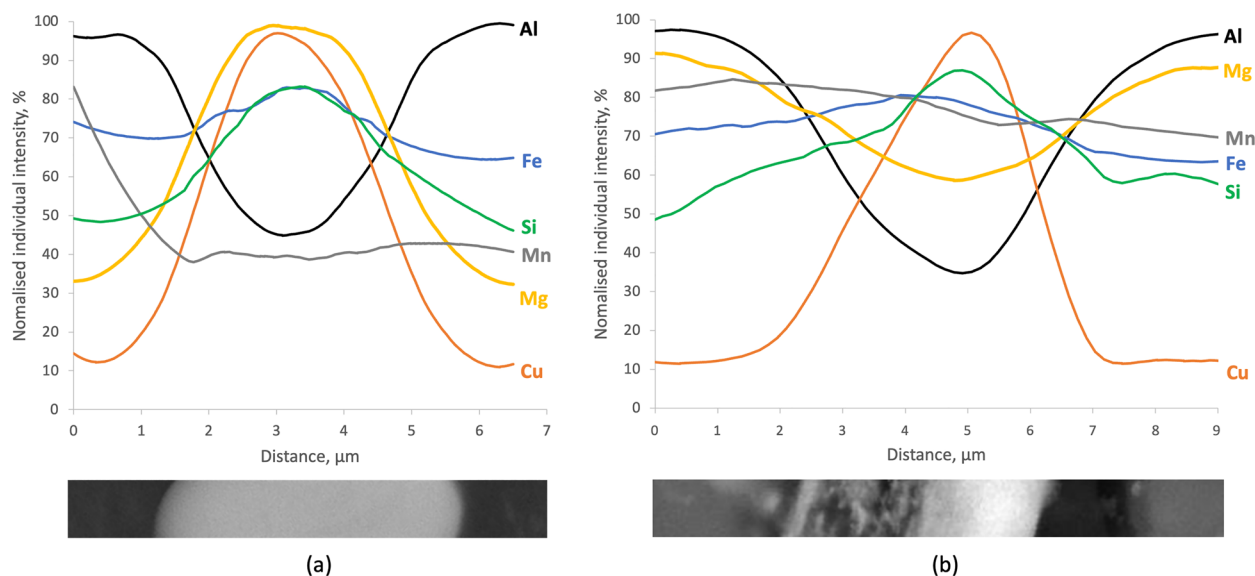
Fig. 14 Modern reference alloy 2024(p)—EDS scan profiles (normalised individual X-ray intensity vs. distance) of the type S particle analysed in Fig. 13: (**a**) before and (**b**) after 19 h of exposure to NaCl 0.01 M solution

particle reduces in size due to the preferential dissolution of the less noble component (Mg) with a corresponding Cu enrichment. As previously mentioned, the change in composition induces a reversal of polarity with respect to the matrix, making the IMP cathodic. During the final phase of the exposure, the basic environment induced precipitation of the oxides/hydroxides, leading to an increase in the oxygen content on the precipitate and in the surrounding areas.

Therefore, in terms of localised corrosion, these results further confirmed a comparable behaviour between historic and modern alloys also on the microscale. This is of paramount importance to help choosing the most representative substrates for further studies on the development of conservation strategies.

Conclusions

In the present work, constituent materials from a North American P-47D Thunderbolt (Republic Aviation Co.), crashed on land in Italy in 1945, were characterised and compared to those from a French Breguet 765 Sahara n°504 64-PH as well as with modern aluminium alloys (2024 and 2017A). Exfoliation susceptibility tests, electrochemical characterisation and localised ageing tests were carried out to assess the representativeness of these modern alloys in simulating the corrosion behaviour of historic ones and to evaluate the role of intermetallic particles (IMPs) in corrosion processes.

The following conclusions can be drawn from this work:

- The Al-based material from the P47-D Thunderbolt consists of the 24S historic alloy, analogous to modern 2024 (Super Duralumin family), both for fuselage plates and structural elements such as stringers. The microstructure showed a slightly higher grain size (and hence slightly lower hardness) and coarser intermetallic particles than the corresponding modern 2024. However, from a qualitative point of view, the main microstructural features of the historic alloy are the same as the modern one. Regarding corrosion morphologies observed in P47-D Thunderbolt samples, exfoliation and pitting were mostly detected in extruded stringers and in rolled plates, respectively.
- Exfoliation test showed that Super Duralumin historic stringers are very susceptible to exfoliation and display a comparable behaviour to the corresponding modern alloy (2024), due to their typical fibrous microstructure with thin elongated grains, induced by severe plastic deformation. The Super Duralumin historic plate from the P47-D Thunderbolt was moderately susceptible to exfoliation as well as the corresponding modern alloy. Conversely, the historic plate from the Breguet 765 Sahara showed a different behaviour in comparison to the modern 2017A: the former was susceptible to exfoliation whilst the latter underwent localised corrosion with crater-like morphologies: The higher susceptibility of the historic plate to exfoliation may be related with its slightly finer and more elongated grain structure.
- Electrochemical characterisation showed that the modern 2017A and 2024 alloys, both rolled and

Martini *et al. Heritage Science* (2024) 12:16

Page 20 of 21

extruded, exhibit very similar corrosion behaviour to the historic ones. Therefore, even though 2017A rolled plates in EXCO tests showed a different corrosion morphology in comparison to the corresponding historic alloy, modern 2017A rolled plates could be used as representative substrates for electrochemical screening of protective treatments and coatings for historic aircrafts.

- Also from a localised corrosion point of view, degradation mechanisms are comparable for both modern and historic 2024 and are driven by microstructural and compositional evolution of intermetallic particles (IMPs). Trenching (*i.e.,* localised dissolution leading to particle undercutting), was observed in both cases, because of the micro-galvanic coupling between the cathodic IMP and the surrounding matrix. During exposure, Mg-rich IMPs are subject to incongruent dissolution of less noble components that induces an inversion of their polarity (from cathodic to anodic).

Consequently, the tests performed on historic and modern alloys to compare their behaviour upon different types of corrosion allowed us to choose, among modern materials, those who could be used as representative and analogous substrates for the development of new strategies for the protection and the conservation of historic aircrafts. Additionally, the collected results allowed to expand the microstructural and compositional dataset of historic aircraft wrecks.

Abbreviations

B	Breguet 765 Sahara n°504 64-PH aircraft
BSE	Backscattered electrons
CP	Constituent particles
d_{max}	Feret diameter
d_{90}	90th percentile feret diameter
E_{BD}	Breakdown potential
E_{cor}	Corrosion potential
E_{oc}	Open circuit potential
EDS	Energy dispersive spectroscopy
EIS	Electrochemical impedance spectroscopy
EXCO	Exfoliation test
f_2	Circularity
FEG	Field emission gun
$HV_{0.3}$	Vickers microhardness (test force: 0.3 kgf (2.942 N))
IA	Image analysis
i_{cor}	Corrosion current
IMP	Intermetallic particle
JPI-CH	Joint programming initiative on cultural heritage
OM	Optical microscopy
OCP	Open circuit potential
P	Thunderbolt P-47D aircraft
p	Plate
PL0	Rolling plane or the plane including the extrusion direction
PL1 and PL2	Transverse orthogonal planes with respect to PL0
PROCRAFT	PROtection and conservation of heritage airCRAFT
R_p	Polarization resistance
s	Stringer
SEM	Scanning electron microscope
TEM	Transmission electron microscope
WWII	Second world war
2024(p)	2024-T3 rolled plate
2024(s)	2024-T3511 extruded stringer
2017A(p)	2017A-T4 rolled plate

References
1. Daly LM. Aviation archaeology of World War II gander: an examination of military and civilian life at the Newfoundland Airport, Doctoral (PhD) thesis. 2015.
2. Brunet M, Robbiola L, Deshayes C, Bernardi E, Martini C, Chiavari C, Balbo A, Monticelli C, Fišer J, Vyhlídal T, Echinard J, Guilminot E. First step in the PROCRAFT Project on WWII Aircraft Heritage: Investigation and Conservation of the AluminiumAlloys. In: Paul Mardikian, Liisa Näsänen and Aki Arponen editors. METAL 2022 - Proceedings of the Interim Meeting of the ICOM-CC Metals Working Group, September 5-9, 2022, Helsinki, Finland, pp. 78–86. ISBN: 978-2-491997-61-8.
3. Ouissi T, Collaveri G, Sciau P, Olivier J-M, Brunet M. Comparison of aluminum alloys from aircraft of four nations involved in the WWII conflict using multiscale analyses and archival study. Heritage. 2019;2:2784–801.
4. Zhao Q, Guo C, Niu K, Zhao J, Huang Y, Li X. Long-term corrosion behavior of the 7A85 aluminum alloy in an industrial-marine atmospheric environment. J Mater Res Technol. 2021;12:1350–9.
5. Sun S, Zheng Q, Li D, Wen J. Long-term atmospheric corrosion behaviour of aluminium alloys 2024 and 7075 in urban, coastal and industrial environments. Corros Sci. 2009;51:719–27.

Martini *et al. Heritage Science* (2024) 12:16

Page 21 of 21

6. Gasquères C, Sarrazin-Baudoux C, Petit J, Dumont D. Fatigue crack propagation in an aluminium alloy at 223 K. Scr Mater. 2005;53:1333–7.

7. Canepa E, Stifanese R, Merotto L, Traverso P. Corrosion behaviour of aluminium alloys in deep-sea environment: a review and the KM3NeT test results. Mar Struct. 2018;59:271–84.

8. Reinhart FM. Corrosion of metals and alloys in the deep ocean, technical report R834. Port Hueneme: Civil Engineering Laboratory, Naval Construction Battalion Center; 1976.

9. Rynewicz JF. Evaluation of paint coatings tested in the deep Atlantic and Pacific Oceans. In: Corrosion in Natural Environments — ASTM STP 558. Philadelphia, PA: American Society for Testing and Materials; 1974. pp. 209–305.

10. Bellou N, Papathanassiou E, Dobretsov S, Lykousis V, Colijn F. The effect of substratum type, orientation and depth on the development of bacterial deep-sea biofilm communities grown on artificial substrata deployed in the Eastern Mediterranean. Biofouling. 2012;28:199–213.

11. Féron D. Corrosion behaviour and protection of copper and aluminium alloys in seawater. EFC 50. Cambridge: Woodhead Publishing; 2007.

12. Yasakau KA, Zheludkevich ML, Ferreira MGS. Chapter 15 - Role of intermetallics in corrosion of aluminum alloys. Smart corrosion protection. In: Rahul Mitra editor. Intermetallic Matrix Composites. Duxford, UK: Woodhead Publishing; 2018. pp.425–462.

13. Vargel C. Corrosion of aluminium. 2nd ed. Amsterdam: Elsevier; 2020.

14. Buchheit RG, Grant RP, Hiava PF, Mckenzie B, Zender GL. Local Dissolution Phenomena Associated with S Phase (Al2CuMg) Particles in Aluminum Alloy 2024-T3. J Electrochem Soc. 1997;144: 2621–2628. https://doi.org/10.1149/1.1837874.

15. Kaufman JG. Corrosion of aluminum and aluminum alloys. In: Cramer Stephen D, Covino Bernard S Jr, editors. Corrosion: materials,Vol 13B, ASM Handbook. Materials Park, OH: ASM International; 2005.

16. Boag A, Hughes AE, Glenn AM, Muster TH, McCulloch D. Corrosion of AA2024-T3 Part I: localised corrosion of isolated IM particles. Corros Sci. 2011;53:17–26.

17. Parvizi R, Tan MY, Hughes AE. Chapter 14 - Recent Insights Into Corrosion Initiation at the Nanoscale. In: Roger N. Lumley editor. Fundamentals of Aluminium Metallurgy. Duxford, UK: Woodhead Publishing; 2018. pp.525–551. https://doi.org/10.1016/B978-0-08-102063-0.00014-X.

18. Birbilis N, Buchheit RG. Electrochemical characteristics of intermetallic phases in aluminum alloys: an experimental survey and discussion. J Electrochem Soc. 2005;152:B140.

19. Kosari A, Tichelaar F, Visser P, Zandbergen H, Terryn H, Mol JMC. Dealloying-driven local corrosion by intermetallic constituent particles and dispersoids in aerospace aluminium alloys. Corros Sci. 2020;177:108947

20. Zhang B, Wang J, Wu B, Oguzie EE, Luo K, Ma XL. Direct observation of atomic-scale origins of local dissolution in Al-Cu-Mg alloys. Sci Rep. 2016;6:39525.

21. Wang J, Zhang B, Zhou YT, Ma XL. Multiple twins of a decagonal approximant embedded in S-Al2CuMg phase resulting in pitting initiation of a 2024Al alloy. Acta Mater. 2015;82:22–31.

22. Bobby Kannan M, Bala Srinivasan P, Raja VS. Chapter 8 - Stress corrosion cracking (SCC) of aluminium alloys. In: V.S. Raja, Tetsuo Shoji editors. Stress Corrosion Cracking. Cambridge, UK: Woodhead Publishing; 2011. pp.307–40.https://doi.org/10.1533/9780857093769.3.307.

23. Mouritz AP. Introduction to aerospace materials. Cambridge, UK: Woodhead Publishing; 2012.

24. Bardal E. Corrosion and protection. London: Springer; 2004.

25. Air Club & Fun - La storia di Loren Hintz. http://airclubfun.it/la-storia-di-loren-hintz. Accessed 27 July 2023.

26. ASTM G34 - 01. Standard Test Method for Exfoliation Corrosion Susceptibility in 2XXX and 7XXX Series Aluminum Alloys (EXCO Test). 2018.

27. Brunet M, Robbiola L, Sciau P, Drieux-Daguerre M. Preserving Aviation Heritage: The Need for an Approach Based on Materials Analysis. In: Claudia Chemello, Laura Brambilla and Edith Joseph editors. METAL 2019 - Proceedings of the InterimMeeting of the ICOM-CC Metals Working Group, September 2-6, 2019, Neuchâtel, Switzerland, ISBN: 978-92-9012-458-0. 2019.

28. Brunet M, Cochard A, Deshayes C, Brouca-Cabarrecq C, Robbiola L, Olivier JM, et al. Study of post-world war II French aeronautical aluminium alloy and coatings: historical and materials science approach. Stud Conserv. 2020;65:103–17.

29. ASTM E112 - 13. Standard test methods for determining average grain size. 2021.

30. Vander Voort GF. Metallography and microstructures. Materials Park, OH: ASM international; 2004.

31. Cochard A, Zhu K, Joulié S, Douin J, Huez J, Robbiola L, et al. Natural aging on Al-Cu-Mg structural hardening alloys—investigation of two historical duralumins for aeronautics. Mater Sci Eng A. 2017;690:259–69.

32. Kaufman JG. Introduction to aluminum alloys and tempers. Materials Park, OH: ASM International; 2000

33. Birbilis N, Zhu YM, Kairy SK, Glenn MA, Nie JF, Morton AJ, et al. A closer look at constituent induced localised corrosion in Al-Cu-Mg alloys. Corros Sci. 2016;113:160–71.

34. Dix, EH Jr. "A L C L A D" A New Corrosion Resistant Aluminum Product, NACA-TN-259. 1927.

35. AlCoA aluminum and its alloys. Aluminum Company of America; 1935. Pittsburgh

36. Birbilis N, Buchheit RG. Investigation and discussion of characteristics for intermetallic phases common to aluminum alloys as a function of solution pH. J Electrochem Soc. 2008;155:117–26.

37. Hughes AE, Boag A, Glenn AM, McCulloch D, Muster TH, Ryan C, et al. Corrosion of AA2024-T3 Part II: co-operative corrosion. Corros Sci. 2011;53:27–39.

38. Aldykewicz J, Isaac HS, Davenport AJ. Investigation of cerium as a cathodic inhibitor for aluminum–copper alloys. J Electrochem Soc. 1995;142:3342–50.

39. Bethencourt M, Botana FJ, Cano MJ, Marcos M, Sánchez-Amaya JM, González-Rovira L. Behaviour of the alloy AA2017 in aqueous solutions of NaCl. Part I: corrosion mechanisms. Corros Sci. 2009;51:518–24.

Publisher's Note